Journal of Materials Chemistry A

Manganese-rich High Entropy Oxides for Lithium-Ion Batteries: Materials Design Approaches to Address Voltage Fade

Journal:	*Journal of Materials Chemistry A*
Manuscript ID	TA-ART-08-2024-005416
Article Type:	Paper
Date Submitted by the Author:	02-Aug-2024
Complete List of Authors:	Huang, Cynthia; Stony Brook University Luo, Jessica; Stony Brook University, Chemistry Mansley, Zachary; Brookhaven National Laboratory, Interdisciplinary Science Kingan, Arun; Stony Brook University Rodriguez Campos, Armando; Stony Brook University, Chemistry Wang, Zhongling; Stony Brook University, Department of Materials Science and Chemical Engineering Marin Bernardez, Edelmy; Stony Brook University, Chemistry Pace, Alexis; Stony Brook University Ma, Lu; Brookhaven National Laboratory, National Synchrotron Light Source II Ehrlich, Steven; Brookhaven National Laboratory Wang, Lei; Brookhaven National Laboratory, Interdisciplinary Science Department Bock, David C.; Honeywell International Inc Buffalo Takeuchi, Esther; Stony Brook University, Materials Science and Engineering Marschilok, Amy; Stony Brook University, Chemistry Zhu, Yimei; Brookhaven National Laboratory Yan, Shan; Brookhaven National Laboratory, Interdisciplinary Science Department Takeuchi, Kenneth; Stony Brook University, Department of Materials Science and Chemical Engineering; Stony Brook University, Department of Chemistry; Brookhaven National Laboratory, Interdisciplinary Science Department

Manganese-rich High Entropy Oxides for Lithium-Ion Batteries: Materials Design Approaches to Address Voltage Fade

Cynthia Huang[1,2]†, Jessica Luo[1,3]†, Zachary Mansley[4], Arun Kingan[1,2], Armando Rodriguez Campos[1,3], Zhongling Wang[1,2], Edelmy J. Marin-Bernardez[1,3], Alexis Pace[1], Lu Ma[5], Steven N. Ehrlich[5], Lei Wang[1,4], David C. Bock[1,4], Esther S. Takeuchi[1,2,3,4], Amy C. Marschilok[1,2,3,4], Yimei Zhu[2,6], Shan Yan[1,4*], Kenneth J. Takeuchi[1,2,3,4*]

1. Institute of Energy: Sustainability, Environment, and Equity, Stony Brook University, Stony Brook, New York, 11794, United States.

2. Department of Materials Science and Chemical Engineering, Stony Brook University, Stony Brook, New York 11794, United States.

3. Department of Chemistry, Stony Brook University, Stony Brook, New York, 11794, United States.

4. Interdisciplinary Science Department, Brookhaven National Laboratory, Upton, NY 11973, United States.

5. National Synchrotron Light Source II, Brookhaven National Laboratory, Upton, NY 11973, United States.

6. Department of Condensed Matter Physics and Materials Science, Brookhaven National Laboratory, Upton, New York 11973, United States.

*corresponding authors (S.Y.) syan@bnl.gov, (K.J.T.) kenneth.takeuchi.1@stonybrook.edu

† CH and JL contributed equally to the manuscript

Abstract

Lithium- and manganese-rich oxides are of interest as lithium-ion battery cathode materials as Mn is earth abundant, low cost, and can deliver high capacity. Herein, a high entropy strategy was used to prepare Mn rich high entropy oxide (HEO) materials including four additional metals in the compositions (Ni, Co, Fe and Al) using a mild co-precipitation method. Two HEOs ($Li_xNi_{0.1}Mn_{0.6}Co_{0.1}Al_{0.1}Fe_{0.1}O_y$, where x=1.5 for HEO-L and x=0.5 for HEO-H) with layered and spinel-layered hybrid structures were investigated where the morphology, elemental composition, structure, atomic level phase distribution, and electrochemistry were determined. The HEO-L samples involves a Li_2TMO_3 layered structure with ~39% stacking faults. HEO-H is a hybrid structure comprised of 80 wt% spinel and 20 wt% $LiMO_2$ layered structure. The high entropy manganese-rich HEO-L showed higher capacity and 93% retention of the average voltage after 100 cycles while HEO-H showed higher capacity retention and near 100% average voltage retention. *Operando* x-ray absorption spectroscopy revealed that the Ni, Co, and Mn are redox active in both materials while the Fe center remains at the Fe^{3+} oxidation state throughout cycling, where the change in the oxidation states for both materials during discharge were consistent with the delivered electrochemical capacity rationalizing the observed electrochemistry.

Introduction

The investigation of battery active materials is motivated by advances in applications and the need for broader functionality. Harnessing configurational entropy in materials design is a recent area of investigation, where high entropy alloys were first introduced in 2004,[1-3] and high entropy multicomponent oxides (HEO) in 2015.[4, 5] HEO materials are defined as multicomponent systems where the phase stability can be estimated using the Gibbs–Helmholtz equation: $\Delta G_{mix}=\Delta H_{mix}-T\Delta S_{mix}$, where ΔG_{mix}, ΔH_{mix}, and ΔS_{mix} are the changes of the Gibbs free energy, mixing enthalpy, and mixing entropy, and T is temperature.[6] The mixing entropy in an ideal case can be expressed as $\Delta S_{mix}=-R\Sigma x_i \ln x_i$, where R is the ideal gas constant and x_i represents the molar fraction of the ith component ($i \geq 5$). A single-phase structure is stabilized by increasing the configurational entropy through including multiple elements, randomly distributed at the same lattice sites.[7] The versatility of this design concept enables tuning of functionality where incorporation of multiple metal cations can result in HEOs with different structures and properties.[8-12] Prior investigations of HEOs as redox active materials in batteries affirm that understanding the redox reaction of each metal in the structure is critical to gain valuable knowledge for future design strategies.[13]

Lithium containing manganese-rich (LMR) active materials with layered structures have drawn attention and been investigated as insertion-based cathode materials for lithium ion batteries due to the earth abundance of manganese and opportunity for lower cost.[14-18] However, change in the voltage profile under cycling reducing the battery's energy output has remained an issue[19-21] for LMRs and has been attributed to structural degradation, mainly caused by phase transitions, transition metal ion migration, and loss of oxygen.[22-25] Two major strategies in the design of LMR materials have been the purposeful inclusion of spinel domains within layered transition metal oxides to improve rate capability and cycling stability and the incorporation of lithium vacancies to reduce irreversible capacity during the first charge.[26, 27] Another strategy to stabilize LMR materials has been doping.[19, 28, 29] For example, a double doping technique in $Li_{1.2}Mn_{0.533}Ni_{0.267}O_2$ was reported incorporating both Nd and Al as co-dopants.[29] However, to the best of our knowledge, there are no detailed studies applying the high entropy strategy to lithium- and manganese-rich cathode materials. Notably, detailed elemental analysis of materials with five or more elements is often absent where the compositions of high entropy materials are inferred from the precursor solution compositions[30 31 32] or energy dispersive spectroscopy measurements.[33]

The motivation for this study is to investigate a high entropy design strategy for lithium rich manganese oxide insertion materials, coupled with a layered-spinel hybrid structure. The specific materials of interest are lithiated manganese-rich high entropy layered oxides including

four additional metals in the compositions (Ni, Co, Fe and Al). Two manganese-based HEO materials $Li_xMn_{0.6}Ni_{0.1}Co_{0.1}Fe_{0.1}Al_{0.1}O_y$ were studied, where the lithium rich composition was layered (x=1.5, HEO-L) and the lithium deficient version was a layered-spinel hybrid (x=0.5, HEO-H). The materials were prepared using a mild aqueous-based co-precipitation synthesis providing atomic level mixing followed by calcination. Detailed characterization of the materials included determination of structure, structural distribution, morphology, and elemental composition. Atomic scale elemental distribution of HEO-L and HEO-H was investigated using advanced transmission electron microscopy (TEM) methods and related to complementary characterization by x-ray powder diffraction (XRD), scanning electron microscopy with energy dispersive x-ray spectroscopy (SEM/EDS), and x-ray absorption spectroscopy (XAS). The composition and oxidation states of HEO-L and HEO-H were determined using inductively coupled plasma-optical emission spectroscopy (ICP-OES) and XAS respectively. The electrochemical evaluation probed the role of the transition metals where moderate voltage limits were selected to minimize oxygen redox. The electrochemical behavior was investigated in lithium-based batteries via cyclic voltammetry, electrochemical impedance spectroscopy (EIS), determination of rate capability, and galvanostatic cycling. In addition, *operando* XAS was utilized to determine the redox activity of each of the transition metals contained in the samples during electrochemical (dis)charge cycling.

Experimental methods

Synthesis: The Mn-rich high entropy oxide materials of $Li_xMn_{0.6}Ni_{0.1}Co_{0.1}Fe_{0.1}Al_{0.1}O_y$ (x=1.5 for HEO-L and x=0.5 for HEO-H) were synthesized via a coprecipitation method by adapting a previously reported synthesis[34] to include our targeted metal elements. Briefly, the metal acetate precursors were dissolved in appropriate ratios and co-precipitated with oxalic acid. The dried solid samples were annealed under air at 450°C and then at 800°C for 20 hours.

Characterization. X-ray powder diffraction (XRD) measurements of the pristine powders were collected using a Rigaku Miniflex X-ray diffractometer with a 600 W Cu Kα X-ray source equipped with a Kβ filter and D/tex Ultra 1D detector. The stack faults in the material were analyzed using the FAULTS profile refinement program in which structures of compounds are described as atomic layers that are connected through stacking vectors.[35] The percentage of stack faults in the system was calculated using the method outlined previously.[36] Rietveld refinement was accomplished using the FULLPROF software[37] and the refinement of the HEO-L was done according to methods consistent with the previous literature.[38, 39] The background was manually fitted by a linear interpolation of selected points and was not refined. A secondary background phase was added due to the presence of $LiAlO_2$ which was generated using the FullProf Suite software. The peak shape was modelled using a pseudo-Voight function and the scale factor, instrument and profile parameters, cell parameters, atomic positions of the TM layer, and stacking

probabilities were refined. The isotropic atomic displacement parameter (B_{iso}) and atomic occupancies were not refined. Rietveld refinement of HEO-H was accomplished using GSAS II.[40] X-ray absorption spectroscopy (XAS) of the pristine powder was conducted at the National Synchrotron Light Source II (NSLS-II) beamline 7-BM at the Mn, Fe, Co, and Ni K-edges at 6539eV, 7112eV, 7709eV, and 8333eV, respectively. All data was merged, normalized, and calibrated in Athena,[41, 42] and the valence of metal centers was evaluated by linear combination fitting (LCF)[43]. The built-in AUTOBK algorithm was used to minimize background below Rbkg = 1.0 Å. EXAFS spectra were fitted with Artemis using theoretical models with FEFF6[44, 45] based on structures determined from the Rietveld refinement results. A k-range of 2 – 11 $Å^{-1}$ and Hanning window (dk = 1) were used for the Fourier transform parameters, and fitting was performed using k^2 weighting. The k^2 weighted $\chi(k)$ signal was left uncorrected for phase shifts. The R-space window for the fitting was defined as either 1.0 – 3.0 Å or 1.0 – 3.5 Å.

The elemental composition of each sample was determined using inductively coupled plasma – optical emission spectroscopy using a ThermoScientific iCap 6300. Scanning electron microscopy (SEM) characterization was carried out with a JEOL JSM-6010PLUS at 10 kV and the energy dispersive x-ray spectroscopy (EDS) maps were collected at 20 kV. Atomic resolution HAADF imaging, high resolution TEM imaging, and diffraction data were principally collected using a JEOL ARM200CF operated at 200 kV with CEOL GmbH double C_s correctors. Supplemental TEM imaging and diffraction data were collected using a JEOL 2100F operated at 200 kV. EDS data and corresponding images were acquired using a FEI Talos with a SuperX EDS detector at 200 kV.

Electrochemical Testing. The cathodes were 70% HEO-L or HEO-H, 20% carbon and 10% PVDF by mass. The coin cells used lithium metal as the anode, the HEO-L or HEO-H electrode as the cathode, and 1M $LiPF_6$ in 3:7 (v/v) ethylene carbonate (EC)/dimethyl carbonate (DMC) electrolyte. The cells were evaluated in the voltage range 2.2-4.5V vs. Li/Li^+ at 30°C using cyclic voltammetry (CV), rate capability testing, and galvanostatic cycling. CV was conducted using a Biologic VSP multichannel potentiostat for ten cycles with a scan rate of 0.1mV/s. Rate capability testing and galvanostatic cycling were conducted using a MACCOR multichannel testing system. Rate capability was tested at five current densities, 25mA/g, 50mA/g, 100mA/g, 200mA/g and back to 25mA/g, for five cycles at each rate. Galvanostatic cycling was tested at current density of 25 mA/g or 100 mA/g after three initial cycles at 25mA/g. A Biologic VSP multichannel potentiostat was used for the collection of the electrochemical impedance spectroscopy data.

***Operando* X-Ray Absorption Spectroscopy** was collected at the National Synchrotron Light Source II (NSLS-II) beamline 7-BM at the Mn, Ni, Co and Fe K-edges. Two electrode cells were fabricated with an active material/carbon black/PVDF (85/10/5) working electrode, separator,

Li metal anode, and 1 M $LiPF_6$ in EC/DMC (30/70) electrolyte. The cells were cycled at 20-30 mA/g between 4.5-2.2 V.

Results and Discussion

Synthesis and Characterization

A co-precipitation approach providing atomic level mixing followed by calcination was used for the synthesis of manganese-rich high entropy layered oxide materials. Two material structures were deliberately pursued where the ratio of monovalent Li^+ ions was adjusted with target compositions of $Li_xMn_{0.6}Ni_{0.1}Co_{0.1}$ $Fe_{0.1}Al_{0.1}O_y$ where x= 1.5 is identified as HEO-L and x= 0.5 is identified as HEO-H. The elemental composition of the products was determined by ICP-OES where the HEO-L material had Li : Mn : Ni : Co : Fe : Al atomic ratios of 1.5 : 0.6 : 0.1 : 0.1 : 0.1 : 0.1 and HEO-H material had ratios of 0.5: 0.6 : 0.1 : 0.1 : 0.1 : 0.1. X-ray absorption near edge spectra (XANES) for the Ni, Mn, Co and Fe K-edges for the HEO-L-and HEO-H products were collected to determine the oxidation state of each transitional metal (TM) center, **Figure 1a-d**. The spectrum of Mn-K edge of HEO-L has edge energy similar to Li_2MnO_3 while HEO-H has slightly lower energy than Li_2MnO_3 (**Figure 1a**). The spectra of the Ni K-edge of HEO-L-and HEO-H closely resemble that of a NiO reference material (**Figure 1b**). The spectrum of Co-K edge of HEO-L closely resembles the spectrum of a $LiCoO_2$ reference material while the spectrum of HEO-H resembles the spectrum of Co_3O_4 (**Figure 1c**). The spectra of Fe-K edge of both HEO-L and HEO-H closely resemble the $LiFeO_2$ reference sample (**Figure 1d**). From linear combination fitting, the oxidation states of the TM centers were estimated (**Table S1**). The oxygen content of the materials was not directly determined, rather it was estimated from the elemental composition ratio and the oxidation state of the metals. Using the oxidation states of the TM obtained from XANES spectra, assuming an oxidation state of Al^{3+} for aluminum and Li^+ for lithium, and the ratios of the elements from ICP-OES, the oxygen content was estimated assuming charge neutrality. Thus, the average composition for HEO-L is assigned as $Li_{1.5}Mn_{0.6}Ni_{0.1}Co_{0.1}Fe_{0.1}Al_{0.1}O_{2.5}$ and HEO-H is assigned as $Li_{0.5}Mn_{0.6}Ni_{0.1}Co_{0.1}Fe_{0.1}Al_{0.1}O_{2.0.}$

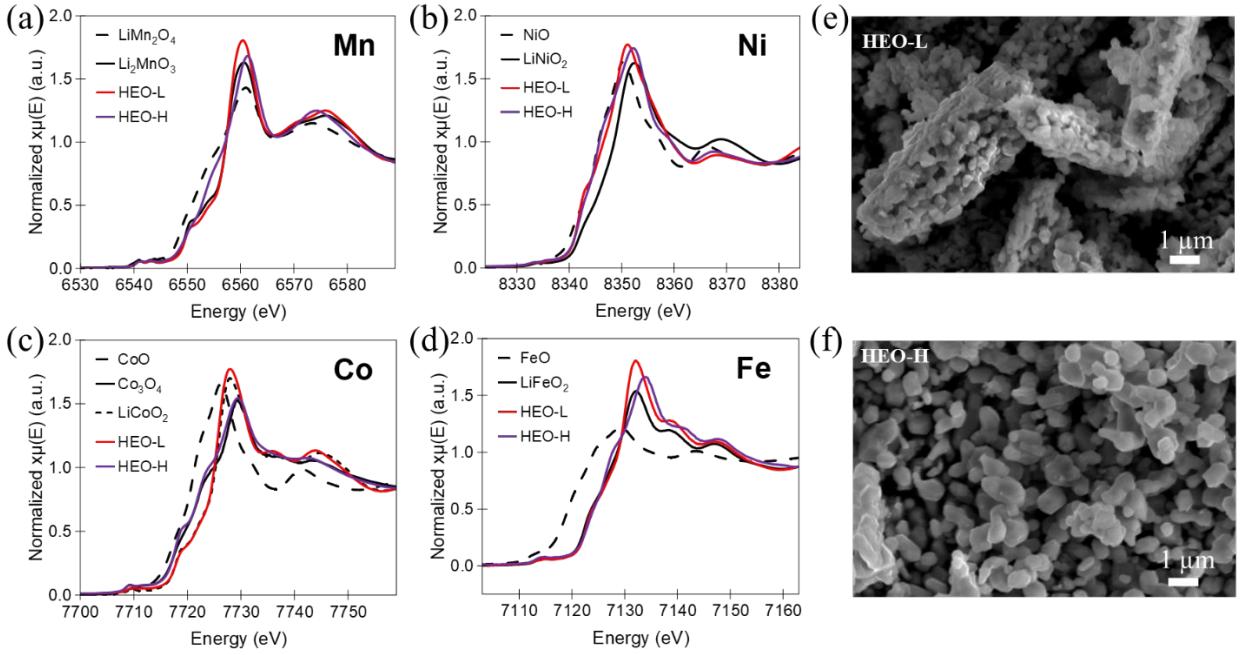

Figure 1. XANES spectra of HEO-L, HEO-H and reference materials at (a) Mn K-edge, (b) Ni K-edge, (c) Co K-edge, (d) Fe K-edge. SEM images of HEO-L(e) and HEO-H (f).

Scanning electron microscopy (SEM) and energy dispersive x-ray spectroscopy (EDS) of the HEO-L and HEO-H samples are shown in **Figures 1e-f** and **S1-2**. SEM images of HEO-L show microbars comprised of nanoparticle composites (**Figure 1e)**, with lengths of 5.7 ± 1.3 μm and widths of 1.7 ± 0.7 μm and the nanoparticles show an average size of 52 ± 14 nm (**Figure S1**). SEM images of HEO-H nanoparticles are shown in **Figure 1f**, where the particles have an average size of 610 ± 190 nm (**Figure S1**). EDS mapping images show uniform Ni, Mn, Co, and Fe distribution with minor Al aggregations in HEO-L and uniform distribution in HEO-H (**Figure S2**).

The structure of HEO-L was characterized by X-ray diffraction (XRD) (**Figure 2**). An asymmetric broadening of the superstructure reflections was observed in the 2θ regions of 20-30° (**Figure 2a**). The broadening of the superstructure reflections has been attributed to stack faults which are described as short range planar defects found in layered materials.[46] To analyze the stack faults in the material, the FAULTS profile refinement program was used in which structures of compounds are described as atomic layers that are connected through stacking vectors.[35] Deviations from the ideal stacking vector result in defects in the material to produce stack faults that are visualized by the broadening of the superlattice peaks in XRD patterns. The monoclinic *C2/m* unit cell of Li_2MnO_3 was transformed to a *P1* triclinic cell, and the TMs were approximated to Mn consistent with previously reported approaches.[39] Two distinct layers were defined: a block

consisting of lithium atoms (L1) and a TM layer consisting of TM, lithium, and oxygen atoms (L2). Two additional layers (L3 and L4) were added that were equivalent to L2 and three stacking vectors, $(\frac{1}{3}, \frac{-1}{3}, \frac{1}{2})$, $(\frac{2}{3}, 0, \frac{1}{2})$, $(0, \frac{-2}{3}, \frac{1}{2})$, were used. The stacking vector of L1→L2 differs from that of L1→L3 and L1→L4 to generate stack faults. In a defect-free structure, only L1→L2 stacking transitions would occur, but presence of L1→L3 and L1→L4 stacking transitions indicate stack faults in the structure, as the scheme illustrates in **Figure 2b-c.** The percentage of stack faults in the system was calculated using a previously outlined method.[36] The refinement plot of HEO-L is shown in **Figure 2a** and the refined parameters and refinement residual values are summarized in **Table S2**. As shown, a good fit was obtained through FAULTS refinement where the fitted profile shows that the primary layered oxide phase is the dominant structure, contributing 99.26% of the area and the $LiAlO_2$ phase contributed only 0.74%. The degree of faulting of the structure was calculated to be ~39%. A schematic of the stacking vectors viewed from the c axis is shown in **Figure S3**.

The structure of HEO-L was further investigated by extended x-ray absorption fine structure (EXAFS) (**Figure 2d-g)**. This approach is complementary to diffraction as it is element specific. Measurements were collected at the K-edges of Mn, Co, Ni, and Fe and the Fourier transformed EXAFS spectra with their corresponding model fits are presented in **Figure 2d-g**. EXAFS modeling of HEO-L was performed using a theoretical model based on the monoclinic Li_2MnO_3 (*C 2/m*) phase a. The model resulted in an excellent statistical fit (R factors below 0.022) at all edges, consistent with the HRTEM and XRD results showing only a Li_2MnO_3 phase. The distances are not corrected for phase shifts and are ca. 0.3–0.4 Å shorter than the interatomic distances determined from theoretical EXAFS modeling. Qualitatively each TM edge exhibit two primary peaks, a 1st shell peak resulting from contributions from nearest neighboring oxygen atoms (TM-O), and a 2nd shell originating from neighboring transition metal, lithium, and oxygen atoms (TM-TM, TM-Li and TM-O). Fitting parameters are tabulated in the supplemental information, **Tables S3-S6**.

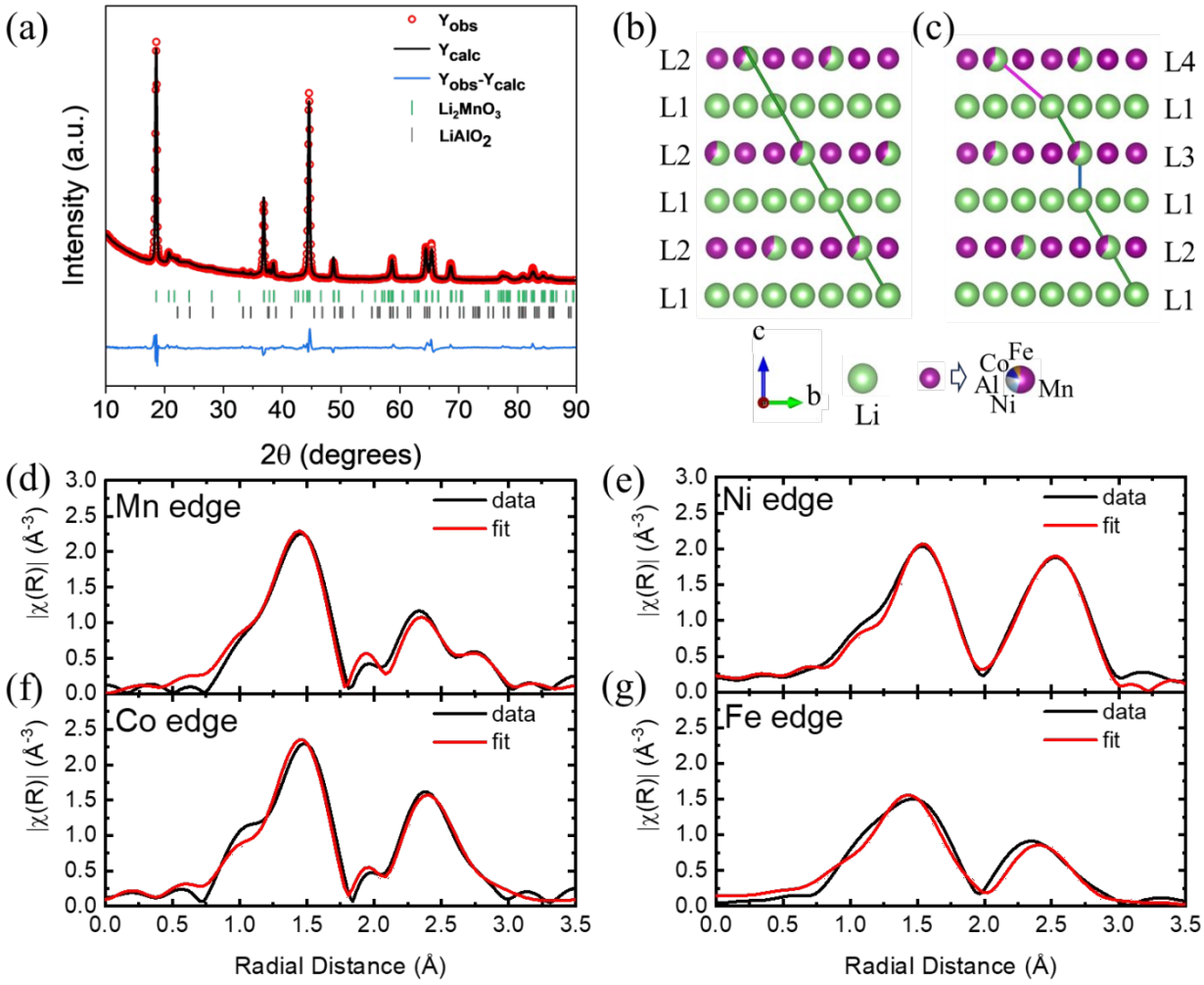

Figure 2. Structural characterization of HEO-L. (a) XRD and Rietveld refinement. (b) Schematic of HEO-L without stack faults. L1 is the lithium layer and L2 is the TM layer. Oxygen atoms were omitted for clarity. Each layer follows the stacking vector (1/3, -1/3, 0.5) shown by the green line. (c) Schematic of HEO-L with stack faults. L2, L3, and L4 are equivalent TM layers, but the stacking vectors for L1 -> L3 (blue line) and L1-> L4 (pink line) are different from L1 ->L2. (d-g) hk^2-weighted $|\chi(R)|$ and corresponding EXAFS fit for the (d) Mn K-edge, (e) Ni-K-edge, (f) Co K-edge and (g) Fe K-edge.

Atomic level characterization of HEO-L was done using transmission electron microscopy (TEM) and energy dispersive spectroscopy (EDS), **Figure 3**. EDS mapping and spectra of HEO-L in **Figure 3a-b** show uniform Ni, Mn, Co, Al, and Fe distribution with minor Al aggregations. A minor variation of composition of different particles was observed relative to the Mn concentrations, with a ratio of Mn to the other metals (Ni, Co, Al and Fe) of 64/36 in region 1 and 73/27 in region 2 (**Figure 3c**). Electron diffraction in **Figure 3d-e** matches well to the Li_2MO_3 structure and shows evidence of long range order in the material in the form of extra diffraction

spots corresponding to a doubled unit cell. The long range order is not present in all particles, as **Figure 3f** shows data from two different particles, one with long range order and one without. The indexed diffraction pattern in **Figure 3e** shows the Li_2MO_3 structure with streaking due to stacking faults consistent with the XRD refinement results.

Atomic resolution HAADF imaging of HEO-L in **Figures 3g-h** corroborate the Li_2MO_3 structure, with some layers displaying irregular atomic ordering as highlighted by yellow circles in **Figure 3g**. The structure contains many defects in the form of stacking faults and point defects. The stacking faults result in orientational changes in the material, as observed in **Figure 3g-h** with representative atomic models in **Figure 3i**. In **Figure 3h**, the top half of the image matches the $[\bar{1}10]$ stacking scheme while the bottom half matches the [100]. The high density of stacking faults is responsible for the streaks observed in the electron diffraction. Point defects are also highlighted in **Figure 3h**, with a substitutional defect of a heavier transition metal into a Li site marked with a red arrow and a regular dimming of the left member of the atomic pairs indicated by the blue arrows. This dimming can result from either vacancies, Li substitution into the site, or preferential occupation of the site by Al atoms which are lighter than the other transition metals.

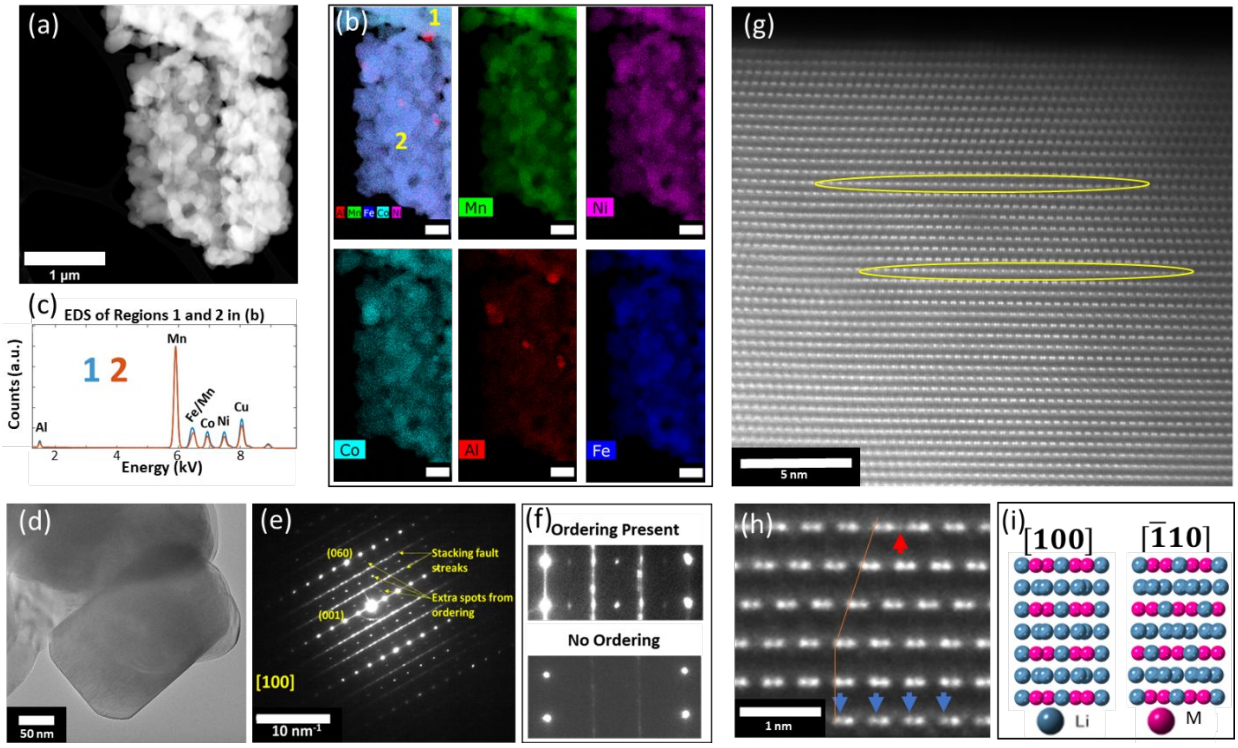

Figure 3. Atomic level characterization of HEO-L. A HAADF image of a HEO-L particle agglomeration is shown in (a) with corresponding EDS maps of the left side of the cluster in (b) and EDS spectra in (c) from the regions marked 1 and 2 in (b). A TEM image of a single HEO-L particle is shown in (d) with a diffraction pattern from the particle in (e). Cropped diffraction patterns from two different particles are shown in (f), with the top pattern containing signal due

to ordering while the bottom indicates no long range order. An atomic resolution HAADF image is shown in (g) with yellow circles highlighting regions with irregular atomic ordering. Another HAADF image is shown in (h) with arrows indicating substitution of a transition metal into a Li site (red arrow), periodic dimming of the left member of the atomic pairs (blue), atomic stacking faults (orange line). Atomic models of the Li_2MnO_3 structure viewed along the indicated zone axes are shown in (i).

The structure and composition of HEO-L were characterized at both bulk and atomic levels using HRTEM, XRD and EXAFS. HEO-L showed a homogeneous Li_2MO_3 layer structure with ~39% stacking faults, some long range order and defects stabilized by the presence of 13% oxygen vacancies that contribute to the configurational entropy of the system and bring the material into a high entropy regime ($\Delta S_{config} \geq 1.5R$).

The structure of HEO-H was probed by X-ray diffraction and EXAFS (**Figure 4**). The refined XRD pattern and the refined crystallographic data are shown in **Figure 4a** and **Table S7,** respectively. HEO-H was fitted using two phases, a layered phase with a $R\bar{3}m$ space group and a spinel phase with a $Fd\bar{3}m$ space group. The refined results indicate that the sample was comprised of 20 wt% layered phase and 80 wt% spinel phase (**Figure 4b)**. The layered phase consists of $LiMO_2$, where Li and TM atoms occupy 3b and 3a Wycoff positions to form alternating Li and TM layers consistent with previous reports of $LiMO_2$ structures.[47] The spinel phase adopts the structure of LiM_2O_4 where Li atoms occupy the tetrahedral 8a site while the transition metals occupy the 16d octahedral site.[48] The (2 2 0) peak can be used to detect cation mixing for LiM_2O_4 spinel. Typically, this peak is not observed when only Li atoms occupy the tetrahedral site due to the low scattering effect of Li atoms.[49] The presence of this peak at 30.8° in HEO-H suggests partial occupation of the tetrahedral site by TMs. Based on the EXAFS findings described below, the atomic occupancies in the XRD refinement of the layered and spinel phase were constrained (**Table S7**), where only Mn and Co were included in the TM layer. Li atoms occupy the 3b site while the TMs occupy the 3a site. The TM occupancies were refined, but the atomic position was constrained to full occupancy. The Li and O occupancy was not refined. For the spinel phase, all positions were also constrained with full occupancy at each site. Li and Co atoms occupy the 8a tetrahedral site with the other TMs occupying the 16d octahedral site. The Li and Co occupancies were refined, but the other TMs were constrained to 60:40 Mn:TM and not refined.

EXAFS modeling was used to assess the local atomic structure of HEO-H. EXAFS augments the X-ray diffraction and TEM results as it allows element specific determination of coordination environment to provide additional insight into these multicomponent materials. The Fourier transformed EXAFS spectra samples and their corresponding fits are presented in **Figure 4c-f** and the fitting parameters are tabulated in the supplemental information, **Tables S8-S11**. The

structural fitting models for the HEO-H sample were developed consistent with the XRD results, which reveal the sample is comprised of both a layered phase with a $R\bar{3}m$ space group and a spinel phase with a $Fd\bar{3}m$ space group. For the spinel phase, both tetrahedral holes (Wyckoff position 8a) and octahedral holes (Wyckoff position 16d) were considered for the position of the central absorbing atom. Modeling using combinations of these phases was attempted at each edge. All scattering paths between the central atom and the various neighboring transition metals in the high entropy materials were modeled using Mn as the neighboring atom. Mn, Co, Ni, and Fe all have similar Z and thus comparable scattering amplitudes and phase shifts;[50] as a result differences in Z could not be reliably distinguished from the fit. At the Mn edge, a model with Mn atoms located in both the layered phase and the octahedral position of the spinel phase results in the best fit. Phase fractions of the layered and spinel phases were 0.85(9) and 0.15(9), respectively, in good agreement with the XRD Rietveld refinement result of layered and spinel phases as 0.80(3) and 0.20(2), respectively. In contrast, analysis of the Co edge reveals that Co atoms occupy the layered phase (phase fraction = 0.71(6)) and the tetrahedral hole of the spinel phase (phase fraction = 0.29(6)). This is consistent with the XRD refinement where TM was observed to be in the tetrahedral site of the spinel phase. Furthermore, Ni and Fe edge analysis suggests that these elements are located primarily in the octahedral site of the spinel phase. Thus, the results provide information about the local environment of each transition metal and indicate that the TM ions are not evenly distributed across the layered and spinel phases of the HEO-H material.

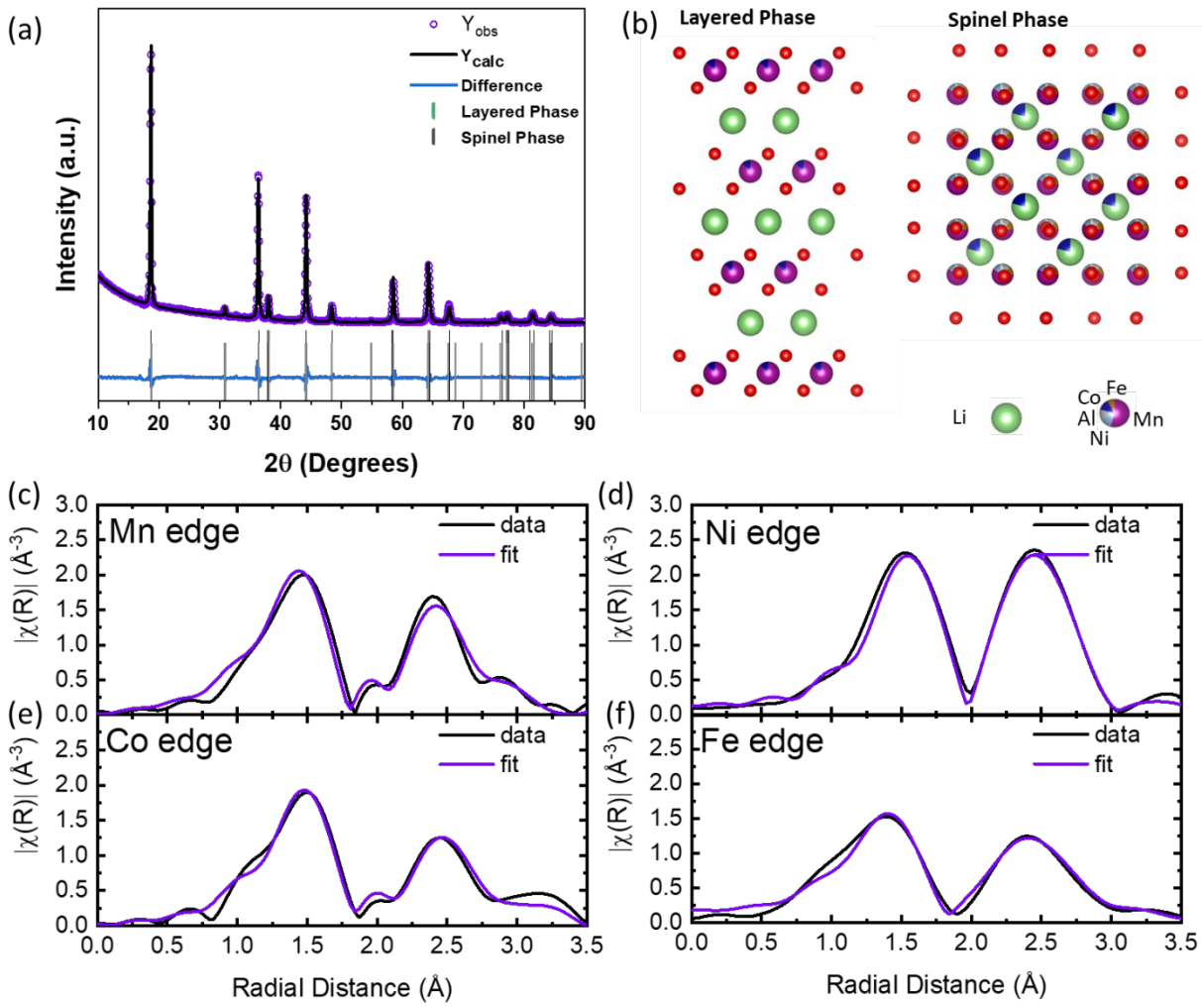

Figure 4. Structural characterization of HEO-H. (a) XRD Rietveld refinement. (b) Schematic spinel structure and $LiMO_2$ layered structure. (c-f) k^2-weighted $|\chi(R)|$ and corresponding EXAFS fit for at the (c) Mn K-edge, (d) Ni-K-edge (e) Co K-edge and (f) Fe K-edge.

TEM images and EDS mapping data from the HEO-H sample are shown in **Figure 5**. EDS mapping and spectra in **Figure 5a-b** show uniform Ni, Mn, Co, Al, and Fe distribution with some minor compositional variation. The sample contains two particle morphologies, rough (**Figure 5c**) and smooth (**Figure 5g**). The rough particles contain multiple grains and a mixture of spinel and $LiMO_2$ layered structures with an approximate 60/40 ratio of Mn to the other metals (Al, Fe, Co, and Ni), while the Mn-rich phase is >90% Mn and adopts the $LiMO_2$ structure as seen in **Figure 5 c-f**. The smooth particles adopt the spinel structure throughout and the elemental distribution is homogeneous. The spinel phase in the smooth particles is observed to be pristine and does not contain internal strain or stacking faults **(Figure 5h)**, while that in the rough particles contains stacking faults and strain **(Figure 5i)**. These results are consistent with XRD refinements and EXAFS fittings.

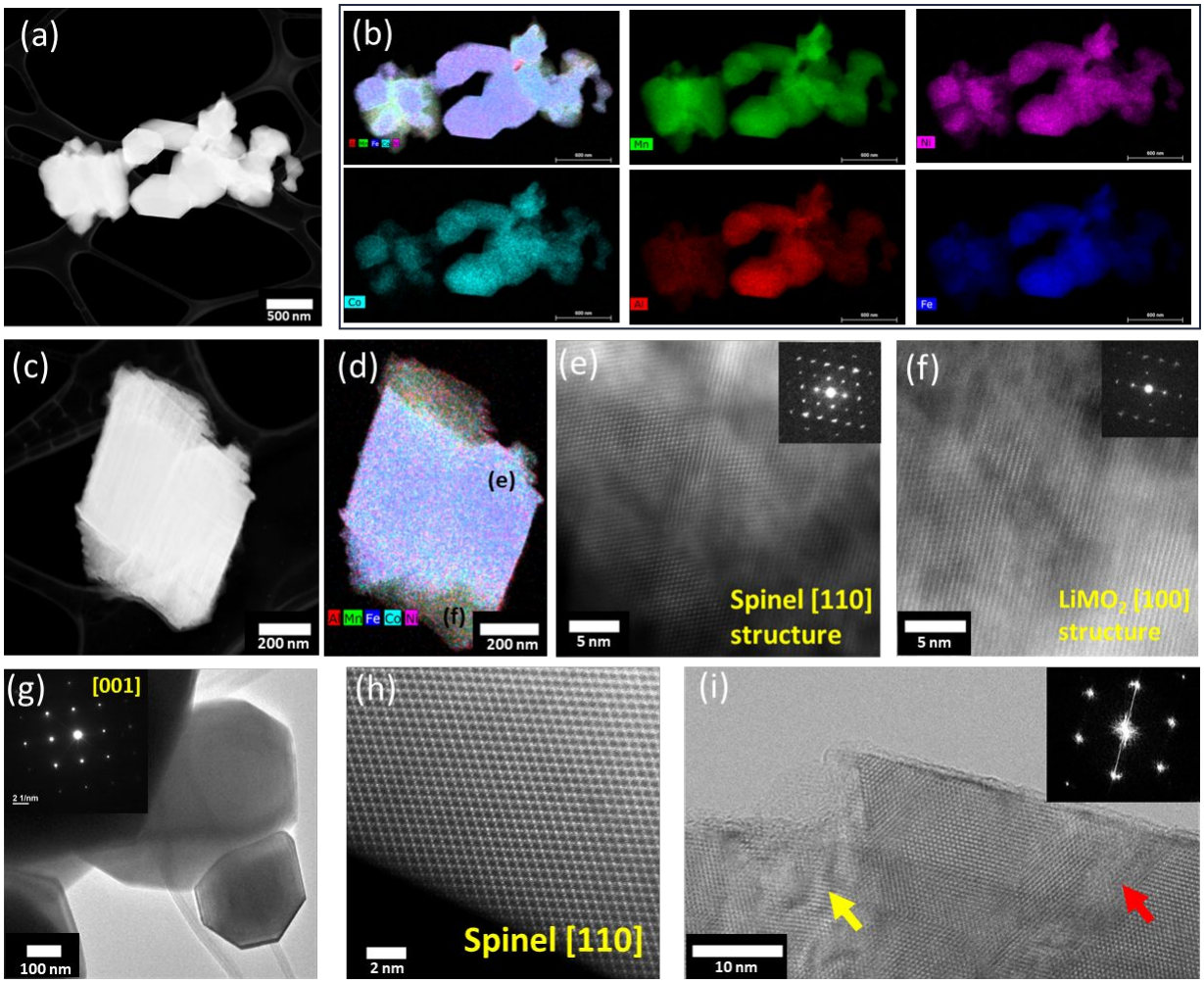

Figure 5. Atomic level characterization of HEO-H. A HAADF image of a particle cluster of HEO-H is shown in (a) with corresponding EDS maps given in (b). A HAADF image and corresponding EDS map of a rough particle are shown in (c) and (d) respectively, and high resolution HAADF images from that particle are shown in (e) and (f) from the regions indicated in (d), where (e) is taken from a region containing the 60/40 elemental ratio with a spinel structure and (f) is from a Mn rich region that displays the $LiMO_2$ structure. A TEM image and inset diffraction pattern in (g) show a smooth particle (bottom right of image) with a spinel structure viewed along the [001] zone axis, and an atomic resolution image of a different smooth particle is shown in (h). A high-resolution TEM image from a spinel region in a rough particle is shown in (i) containing stacking faults (red arrow) and strain (yellow arrow).

Electrochemistry of HEO-L and HEO-H

The electrochemistry of HEO-L and HEO-H was evaluated in two electrode cells versus lithium metal (**Figure 6**). Cyclic voltammetry (CV) was conducted over a voltage window of 4.5-2.2 V versus Li/Li^+ and a scan rate of 0.1 mV/s. The CV of the HEO-L sample shows a minor

redox couple at 3.3 / 3.0 V whose peak current increased with cycle number and a major redox couple at 4.1/3.9 V whose peak current decreased with cycling (**Figure 6a**) indicating structural evolution with cycling. The CV of HEO-H shows redox coupled peaks at 2.9/3.0 V and at 4.0/4.1 V where the peak currents of the lower voltage couple increase with cycle number, and while those at 4.0/4.1 V remain unchanged (**Figure 6d**).

Galvanostatic cycling of HEO-L in a voltage window of 4.5-2.2 V versus Li/Li^+ at 25 mA/g showed two-phase regions, with plateaus appearing ~3.0 and 4.0 V where the high voltage plateau slightly decreased in capacity with cycling while the low voltage plateau increased consistent with the evolution of the peak currents in the CV (**Figure 6b)**. The dQ/dV plots of the HEO-L voltage profiles show an oxidation peak at 4.0 V and an emerging peak at 4.5 V during the initial charge while three small reduction peaks at 2.75, 3.45 and 4.0 V and two oxidation peaks at 3.0 and 4.2 V are seen in subsequent cycles (**Figure 6c**). Notably, the peak at 4.5 V was only present in the first cycle. For HEO-H, the discharge voltage profile shows two voltage plateaus at ~2.7 and 4.1 V (**Figure 6e**). The dQ/dV plot of HEO-H shows a major redox couple at 2.7/2.9 V and a lower peak current redox couple at 4.0 V (**Figure 6f**). The peak intensity at 2.7 V increased with cycling while other peak intensities remain unchanged.

The irreversible capacity for cycles 1 and 2 was assessed for both the HEO-L sample and the HEO-H sample (**Figure S13**). The irreversible capacity for HEO-L was 34 mAh/g for cycle 1 and 12 mAh/g for cycle 2 where the charge capacity exceeded the discharge capacity under the 25 mA/g current level. In contrast, the HEO-H sample showed a negative irreversible capacity on cycle 1, where the charge capacity was lower than the discharge capacity by 36 mAh/g indicative of the limited lithium ion supply in the parent structure. The irreversible capacity on cycle 2 was 4 mAh/g. In comparison of the irreversible capacities for the two material types, the HEO-H material shows suppressed irreversible capacity consistent with the hybrid layered-spinel strategy previously employed for LMR.[26, 27] However, the negative irreversible capacity on cycle 1 in these data indicates low levels of active lithium cation in the parent HEO-H material. Comparing the irreversible capacity values for cycle 2 as a percentage of the initial charge, the values are lower for HEO-H at 5.4% compared to 9% for the HEO-L material consistent with the greater lithium vacancies in the HEO-H structure.

The extended cycle life of HEO-L and HEO-H at 25 mA/g is shown in **Figure 6g-i**. HEO-L had an initial discharge capacity of 112 mAh/g and 120 mA/g at the 100^{th} cycle with a capacity retention of 107% (**Figure 6g**). The average voltage for the first discharge was 3.48 V and was 3.25V at 100^{th} cycle showing an average voltage retention of 93% (**Figure 6h**). The energy delivery was 390 mWh/g at first cycle and 390 mWh/g at 100^{th} cycle indicating a capacity retention of 100% (**Figure 6i**). HEO-H showed an initial discharge capacity of 78 mAh/g where the delivered capacity steadily increased delivering 91 mAh/g at the 100^{th} cycle with a capacity

retention of 117% (**Figure 6g**). Examination of the average voltage indicated an average discharge voltage of 3.14 V for the first cycle and 3.12 V for cycle 100 with an average voltage retention of near 100% (**Figure 6h**). The energy delivered in the first cycle was 245 and 285 in the 100th cycle with a retention of 106% (**Figure 6h**). Similar features were observed under extended cycling at 100 mA/g for HEO-H and HEO-L cells (**Figure S4**). Thus, the HEO-H spinel structured material did result in enhanced capacity retention. Additional cycling was conducted for HEO-L at a current level of 10 mA/g of active material (**Figure S5**). The initial charge capacity was 200 mAh/g and the initial discharge capacity was 160 mAh/g rising to 175 mAh/g at cycle four indicating that the samples show rate limitations and deliver higher capacities at lower rate.

HEO-L and HEO-H were evaluated at a series of higher currents to compare the rate capability beginning with 25 mA/g followed by 50, 100, 200, and then returning to 25 mA/g where each test was run for five cycles. The HEO-L sample consistently delivers higher capacity thant the HEO-H sample at each rate tested (**Figure S6a**). Interestingly, the materials show similar rate capability when the capacity is normalized (**Figure S6b).** While the delivered capacity of the HEO-L is higher than the HEO-H materials, the relative capacity retention with increasing rate is similar. The relative capacity retention is around 80, 70 and 60% at current levels of 50, 100 and 200 mA/g for each of the samples. Notably, the capacity retention under the second set of 25 mA/g cycles is lower for the HEO-L sample than that of the HEO-H sample.

Based on the electrochemical behavior for the materials studied here, the delivered capacity under galvanostatic discharge is compared with examples from the literature of related materials of layered, spinel, and layered-spinel hybrid structures (**Table S12**). **Table S12** also indicates the synthetic approaches used to prepare each of the materials where the materials have been prepared by a variety of methods including solid state, sol-gel, co-precipitation, hydrothermal, and combustion. In comparing the electrochemical charge capacities and delivered capacities there are several notable observations. First, the majority of reports on these material types use cells charged to voltage >4.5V to access oxygen redox, thus we estimated charge capacity up to 4.5V on the first charge for inclusion in the table for a more direct comparison along with reporting the full charge capacity. In most cases the currents used for the studies were 10 mA/g or less suggesting that the materials show some kinetic limitations reminiscent of the materials tested here. Typically, the layered materials deliver higher capacity than the spinel structured materials. The reports of the layer-spinel hybrid materials indicate charge to 4.8-4.95V, however, by using estimates of cells charged to 4.5V the capacities are generally lower than the layered materials. The capacities delivered, as reported here for the HEO-L and the lower capacity HEO-H evaluated under a more limited voltage range, are comparable in terms of functional capacities based on prior reports.

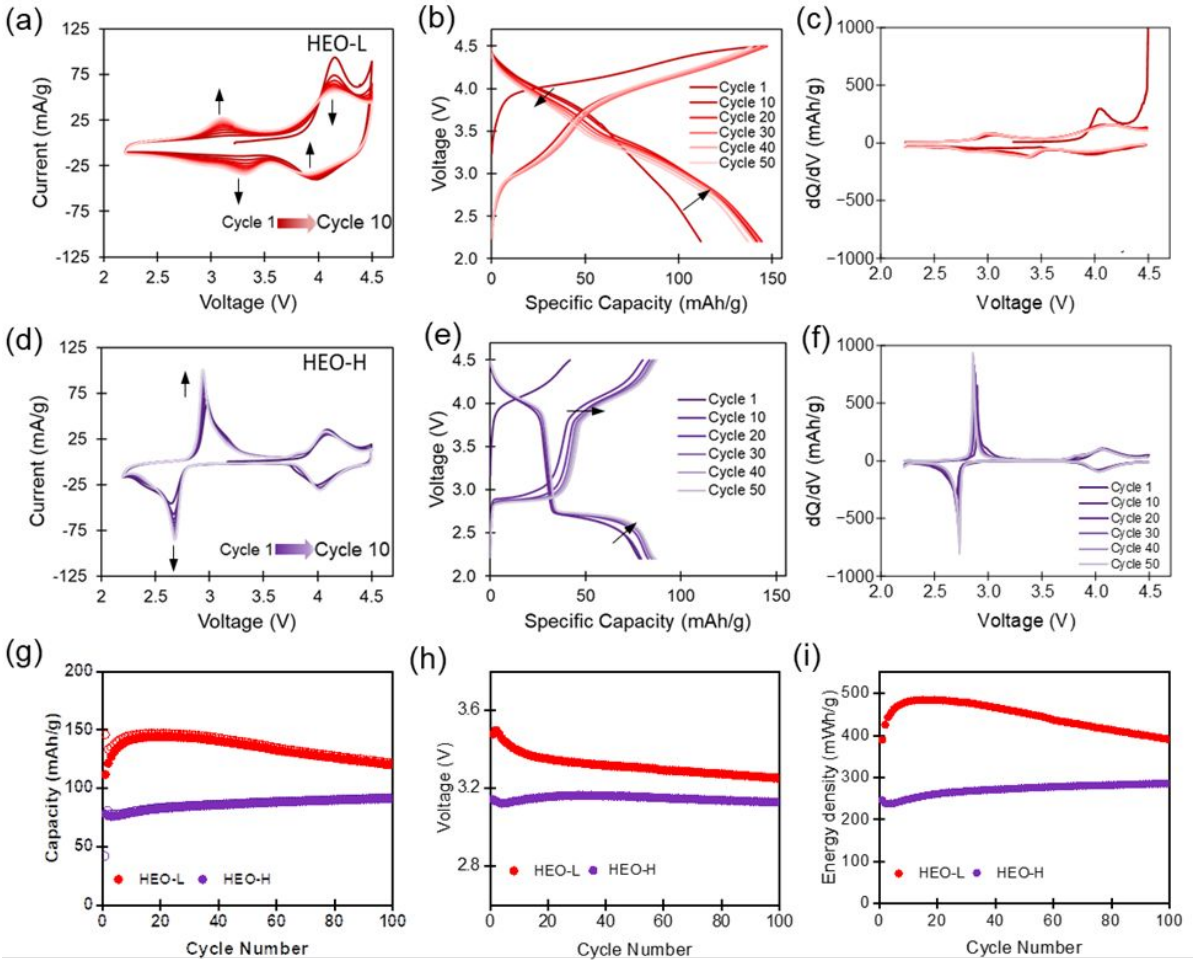

Figure 6. Electrochemistry of HEO-L (red) and HEO-H (purple). (a) CV, (b) voltage profiles, (c) dQ/dV of HEO-L at 25 mA/g. (d) CV, (e) voltage profile and (f) dQ/dV of HEO-H at 25 mA/g. (g) Extended cycle life of HEO-L and HEO-H, open circle indicates charge and solid cycle indicate discharge. (h) Average voltage of HEO-L and HEO-H. (i) Energy density for discharge of HEO-L and HEO-H.

The electrochemical impedance spectroscopy was recorded for HEO-L and HEO-H after rate capability testing and after galvanostatic cycling for 100 cycles at current levels of 25 and 100 mA/g (**Figure S7**). The impedance as displayed in Nyquist plots indicates the charge transfer resistance of the HEO-L cells is higher before cycling than that of the HEO-H cells. After rate capability testing of 25 cycles (**Figure S5**), there is minor change in the impedance signatures where the charge transfer resistance of the HEO-L sample increased slightly while that of the HEO-H sample decreased. The increase in impedance for HEO-L is consistent with the decreased delivered capacity for the HEO-L sample relative to the HEO-H sample in the second round of 25 mA/g cycling as part of the rate capability test. The changes after galvanostatic cycling are more dramatic. After 100 cycles at 25 mA/g the charge transfer resistance of the HEO-L sample more

than doubles increasing from ~ 220 to ~550 ohms. In contrast, the charge transfer resistance of the HEO-H sample decreases substantially where the impedance is initially at 100 ohms and decreases to 50 ohms after cycling. The differences remain significant after cycling at 100 mA/g where the impedance for the HEO-L sample remains similar ~180 ohms before and after cycling while the impedance of the HEO-H sample decreases significantly from ~140 to 40 ohms after test.

HEO-L exhibited minimal voltage fade despite the intrinsic defects in the structure. It has been suggested that doping Li-rich layered cathodes with different metals can mitigate voltage fade by reinforcing structural stability.[46, 51] The inclusion of additional metals such as Al and Fe in HEO-L may have provided additional structural support by preventing the migration of TM metals to the Li layer.

The HEO-H material consists of a spinel-layer composite and because the spinel phase dominates its composition, it is expected that most of the capacity is due to Li insertion/extraction from the spinel phase.[52] The 2.7 V plateau has also been previously related to a phase transition of the cubic spinel to a tetragonal spinel structure in related materials. A study of a $LiMn_{1.5}Ni_{0.5}O_4$ spinel attributed this peak to the insertion of Li ions into the empty *16c* Wyckoff site of the cubic spinel structure that caused a phase transformation to a tetragonal spinel.[53] Another report on Li and Mn rich hybrid spinel-layered composite cathodes ($xLi[Li_{0.2}Mn_{0.6}Ni_{0.17}Co_{0.03}]O_2$–$(1-x)$ $Li[Mn_{1.5}Ni_{0.425}Co_{0.075}]O_4$) reported the 2.7 V plateau to be associated with the insertion and extraction of Li into the empty octahedral sites of the cubic spinel structure while the 4.1 V voltage plateau was associated with Li insertion and extraction of the 8a tetrahedral sites.[52] The capacity extracted from the sloping region between 3.0 – 4.0 V was attributed to Li (de)intercalation from the layered phase in the prior report. The high capacity retention of HEO-H herein may be attributable to the ability of Li insertion/extraction of the empty *16c* sites of the cubic spinel phase.

Electrochemistry Probe of HEO-L and HEO-H

The oxidation state evolution of Mn, Ni, Co, and Fe for HEO-L and HEO-H lithium cells under galvanostatic cycling as determined by *Operando* XAS is shown in **Figure 7**. The (de)lithiation electrochemistry of HEO-L and the x-ray absorption near edge spectroscopy (XANES) at the Mn, Ni, Co and Fe K-edges is summarized (**Figures 7a and S8**). The XANES spectra were collected during the 1st charge, 1st discharge, and 2nd charge at 30 mA/g in a voltage window of 2.2-4.5V (**Figure 7 and S8**). The Mn edge of pristine HEO-L was stable during the 1st charge, but a small shift to higher energy was observed during the 1st discharge and shifted back during 2nd charge. The edge energy of Ni of pristine HEO-L shifted significantly to higher energy to reach a Ni oxidation state of 3.7+ during charge and shifted back to lower energy during discharge. The Co edge position of HEO-L was close to $LiCoO_2$ and resembled charged $LiCoO_2$ with a Co oxidation state of 3.6+ during the 1st charge and showed reversible energy shifts during

the 1st discharge and 2nd charge. The Fe edge position of HEO-L stayed at the location of the pristine material during cycling.

Linear combination fitting of the XANES data was used to determine the oxidation state evolution as a function of voltage for Ni, Mn, Co, and Fe (**Figure 7a**). The pristine HELO-L showed Mn^{4+}, remained unchanged during the first charge but reached 3.8+ during discharge to 2.2 V. The Mn center was reversibly oxidized during the second charge to Mn^{4+}. The oxidation state of pristine HELO-L showed $Ni^{2.4+}$ that was oxidized to 3+ when charged to 4.25 V and then remained unchanged during the charge from 4.25-4.5 V. During discharge, Ni^{3+} remained until the cell reached 4.0 V, and was reduced to ~2.4+ during the discharge from 4.0 to 2.2 V. The Ni center was oxidized to Ni^{3+} when charged to 4.0 V. The Co oxidation state evolution of HEO-L follows a similar trend to the Ni oxidation state where a $Co^{2.7+/3.0+}$ reversible reaction was observed during (dis)charge. The Fe oxidation states of HEO-L remain at ~3+ with minimum change.

The capacity of the HEO-L during the 1st charge, 1st discharge, and 2nd charge was estimated using only the oxidation state change of Mn, Ni, Co, and Fe centers and was found to be 53, 65, and 46 mAh/g while the corresponding electrochemical capacities were 116, 69, and 69 mAh/g respectively. The data indicate reasonable agreement between the changes in metal oxidation state and the delivered capacity for discharge indicating that transition metal reduction is the major Faradaic process during discharge. However, on charge, the changes in the oxidation states of the transition metal centers do not account for the capacity where there are significant differences both for the first and second charge. The discrepancies suggest participation of additional processes in the electrochemistry in addition to oxidation of transition metal centers, likely oxygen redox activity that can occur under charge particularly to high voltage.[54, 55]

Operando XANES spectra were collected on lithium/HEO-H cells during the 1st charge, 1st discharge, and 2nd charge at 18 mA/g in voltage window of 2.2 - 4.5 V (**Figure 7b**). The oxidation state changes of HEO-H are less pronounced than those observed in HEO-L. A $Mn^{3.7+/3.8+}$ oxidation state change of HEO-H was observed in the first charge and was reduced to $Mn^{3.3+}$ at end of the 1st discharge to 2.2 V. The Co oxidation changed from $Co^{2.6+/2.7+}$ on charge and was reduced to $Co^{2.3+}$ on discharge. $Ni^{2.4+}$ was oxidized to $Ni^{2.5+}$ on charge and reduced to $Ni^{2.2+}$ on discharge. The Fe oxidation state remained at Fe^{3+} throughout.

The electrochemical capacity of the HEO-H is compared to the capacity determined from the oxidation state change of Mn, Ni, Co, and Fe centers for XAS. The electrochemical capacities were 30 mAh/g for the first charge and 102 mAh/g for the 1st discharge. The corresponding capacities estimated from the *operando* XAS data are 14 mAh/g for charge and 93 mAh/g for discharge. The data show good agreement between the changes in metal oxidation state and the delivered capacity for discharge where transition metal reduction is the major Faradaic process during discharge. However, on charge, the oxidation states of the transition metal centers in the HEO-H material during the 1st charge show lower levels of oxidation state change compared to the

electrochemistry suggesting additional processes likely oxygen redox. Interestingly, for HEO-H, the electrochemical capacity under the second charge was 100 mAh/g and the capacity estimated from the XANES data was 96 mAh/g showing reasonable agreement. The decrease in the other reactions taking place such as oxygen redox further rationalize the capacity retention of the HEO-H material.

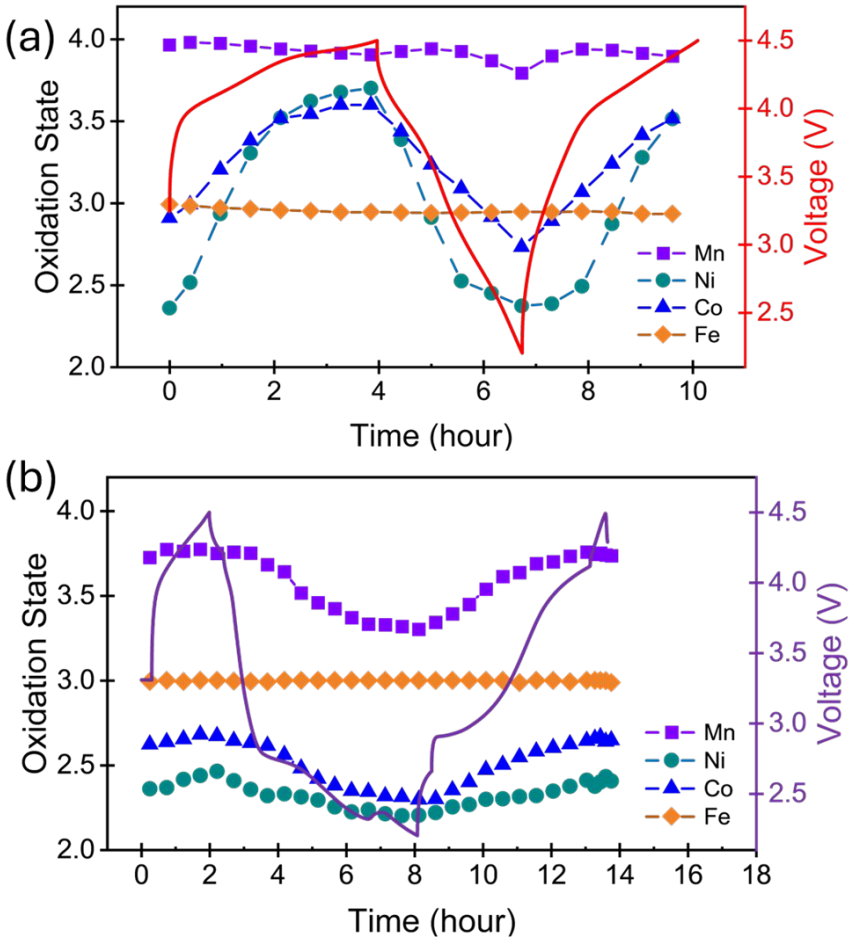

Figure 7. The oxidation state evolution of transition metals along with galvanostatic cycling during *Operando* XAS measurements of (a) HEO-L and (b) HEO-H electrodes in Li half cells.

Conclusion

In this work, Mn rich HEO materials including four additional metals in the compositions (Ni, Co, Fe and Al) were prepared using a mild co-precipitation method. Specifically, two Mn-rich high entropy oxides ($Li_xNi_{0.1}Mn_{0.6}Co_{0.1}Al_{0.1}Fe_{0.1}O_y$, where x=1.5 for HEO-L and x=0.5 for HEO-H) were prepared, with layered and spinel-layered hybrid structures. The morphology, elemental composition, structure, atomic level phase distribution, and electrochemistry of HEO-L and HEO-H were investigated over multiple length scales. At the local level, compositional homogeneity of transition metal centers was affirmed using TEM EDS. Atomic resolution imaging using TEM methods revealed the presence of stack faults in the HEO-L material and localized stacking faults and strain in the HEO-H material. The composition $Li_{1.5}Mn_{0.6}^{4.0+}Ni_{0.1}^{2.4+}Co_{0.1}^{3.0+}Fe_{0.1}^{3.0+}Al_{0.1}O_{2.5}$ of HEO-L involves a Li_2TMO_3 layered structure with ~39% stacking faults stabilized by the presence of oxygen vacancies. The composition of $Li_{0.5}Mn_{0.6}^{3.8+}Ni_{0.1}^{2.4+}Co_{0.1}^{2.7+}Fe_{0.1}^{3.0+}Al_{0.1}O_{2.0}$ of HEO-H is a hybrid structure comprised of 80 wt% spinel with Mn, Ni, and Fe located primarily in the octahedral sites and Co at the tetrahedral site and 20 wt% $LiMO_2$ layered structure with Mn and Co in the transition metal layer as determined from combined analysis by XRD and EXAFS.

Notably, both the high entropy manganese-rich oxides showed minor voltage fade upon extended electrochemical (dis)charge cycling. The high entropy manganese-rich HEO-L showed higher capacity while HEO-H showed higher capacity retention. The HEO-L material displayed voltage retention of 93% after 100 cycles while the HEO-H material showed voltage retention of near 100%. The charge transfer resistance of the HEO-L material increased with cycling while that of the HEO-H decreased contributing to the capacity fade for HEO-L and capacity increase with cycling for HEO-H. *Operando* XANES results revealed that the Ni, Co, and Mn are redox active in both materials while the Fe center remains at the Fe^{3+} oxidation state throughout cycling, where the change in the oxidation states for both materials during discharge were consistent with the delivered electrochemical capacity. This investigation of high entropy manganese-rich oxide contributes to understanding the structure and electrochemical behavior of complex cathode materials, toward development of future batteries with reduced voltage fade and improved capacity retention.

Conflicts of Interest

There are no conflicts of interest to declare.

Acknowledgements

This work was supported as part of the Center for Mesoscale Transport Properties, an Energy Frontier Research Center supported by the U.S. Department of Energy, Office of Science, Basic Energy Sciences via grant No. DE-SC0012673. The microscopy work was conducted at the Brookhaven National Laboratory, which is supported by the U.S. Department of Energy, Basic Energy Sciences, Materials Science and Engineering Division, under Contract No. DE-SC0012704. The synchrotron measurements were conducted at the National Synchrotron Light Source II (NSLS-II) which is a U.S. DOE Office of Science Facility, at Brookhaven National Laboratory under Contract No. DE-SC0012704. E.J.M.B. acknowledges the support of the National Science Foundation Graduate Research Fellowship under grant no. 2234683. E.S.T. acknowledges support from the William and Jane Knapp Chair in Energy and the Environment.

References

1. J. W. Yeh, S. K. Chen, S. J. Lin, J. Y. Gan, T. S. Chin, T. T. Shun, C. H. Tsau and S. Y. Chang, *Advanced Engineering Materials*, 2004, **6**, 299-303.

2. B. Cantor, I. T. H. Chang, P. Knight and A. J. B. Vincent, *Materials Science and Engineering: A*, 2004, **375-377**, 213-218.

3. D. B. Miracle and O. N. Senkov, *Acta Materialia*, 2017, **122**, 448-511.

4. C. M. Rost, E. Sachet, T. Borman, A. Moballegh, E. C. Dickey, D. Hou, J. L. Jones, S. Curtarolo and J.-P. Maria, *Nature communications*, 2015, **6**, 1-8.

5. D. Bérardan, S. Franger, A. K. Meena and N. Dragoe, *Journal of Materials Chemistry A*, 2016, **4**, 9536-9541.

6. Y. Sun and S. Dai, *Sci Adv*, **7**, eabg1600.

7. Y. Ma, Y. Ma, Q. Wang, S. Schweidler, M. Botros, T. Fu, H. Hahn, T. Brezesinski and B. Breitung, *Energy & Environmental Science*, 2021, **14**, 2883-2905.

8. A. Sarkar, Q. Wang, A. Schiele, M. R. Chellali, S. S. Bhattacharya, D. Wang, T. Brezesinski, H. Hahn, L. Velasco and B. Breitung, *Advanced Materials*, 2019, **31**, 1806236.

9. A. Sarkar, B. Breitung and H. Hahn, *Scripta Materialia*, 2020, **187**, 43-48.

10. M. Anandkumar and E. Trofimov, *Journal of Alloys and Compounds*, 2023, **960**, 170690.

11. Q. Wang, L. Velasco, B. Breitung and V. Presser, *Advanced Energy Materials*, 2021, **11**, 2102355.

12. B. S. Murty, J. W. Yeh and S. Ranganathan, in *High Entropy Alloys*, eds. B. S. Murty, J. W. Yeh and S. Ranganathan, Butterworth-Heinemann, Boston, 2014, DOI: https://doi.org/10.1016/B978-0-12-800251-3.00002-X, pp. 13-35.

13. K. Wang, W. Hua, X. Huang, D. Stenzel, J. Wang, Z. Ding, Y. Cui, Q. Wang, H. Ehrenberg, B. Breitung, C. Kübel and X. Mu, *Nature Communications*, 2023, **14**, 1487.

14. K. A. Jarvis, Z. Q. Deng, L. F. Allard, A. Manthiram and P. J. Ferreira, *Chem Mater*, 2011, **23**, 3614-3621.

15. S. Q. Liu, B. Y. Wang, X. Zhang, S. Zhao, Z. H. Zhang and H. J. Yu, *Matter-Us*, 2021, **4**, 1511-1527.

16. B. Ammundsen and J. Paulsen, *Advanced Materials*, 2001, **13**, 943.

17. H. J. Yu and H. S. Zhou, *J Phys Chem Lett*, 2013, **4**, 1268-1280.

18. J. M. Zheng, P. H. Xu, M. Gu, J. Xiao, N. D. Browning, P. F. Yan, C. M. Wang and J. G. Zhang, *Chem Mater*, 2015, **27**, 1381-1390.

19. J. R. Croy, M. Balasubramanian, K. G. Gallagher and A. K. Burrell, *Accounts of Chemical Research*, 2015, **48**, 2813-2821.

20. A. Gutierrez, D. Tewari, J. Chen, V. Srinivasan, M. Balasubramanian and J. R. Croy, *Journal of The Electrochemical Society*, 2023, **170**, 030509.

21. J. Zheng, S. Myeong, W. Cho, P. Yan, J. Xiao, C. Wang, J. Cho and J.-G. Zhang, *Advanced Energy Materials*, 2017, **7**, 1601284.

22. H. Koga, L. Croguennec, M. Ménétrier, P. Mannessiez, F. Weill and C. Delmas, *J Power Sources*, 2013, **236**, 250-258.

23. J. R. Croy, K. G. Gallagher, M. Balasubramanian, B. R. Long and M. M. Thackeray, *Journal of the Electrochemical Society*, 2014, **161**, A318-A325.

24. M. Gu, I. Belharouak, J. M. Zheng, H. M. Wu, J. Xiao, A. Genc, K. Amine, S. Thevuthasan, D. R. Baer, J. G. Zhang, N. D. Browning, J. Liu and C. M. Wang, *Acs Nano*, 2013, **7**, 760-767.

25. E. Hu, X. Yu, R. Lin, X. Bi, J. Lu, S. Bak, K.-W. Nam, H. L. Xin, C. Jaye, D. A. Fischer, K. Amine and X.-Q. Yang, *Nature Energy*, 2018, **3**, 690-698.

26. J. R. Croy, A. Gutierrez, M. He, B. T. Yonemoto, E. Lee and M. M. Thackeray, *J Power Sources*, 2019, **434**, 226706.

27. W. Huang, M. Zhang, M. Ge, S. Li, L. Xie, Z. Chen, G. Wang, J. Lin, J. Qiu and L. Yu, *ACS Energy Letters*, 2023, **8**, 901-908.

28. S. Liu, Z. Liu, X. Shen, X. Wang, S. C. Liao, R. Yu, Z. Wang, Z. Hu, C. T. Chen and X. Yu, *Advanced Energy Materials*, 2019, **9**, 1901530.

29. W. Jiang, C. Zhang, Y. Feng, B. Wei, L. Chen, R. Zhang, D. G. Ivey, P. Wang and W. Wei, *Energy Storage Materials*, 2020, **32**, 37-45.

30. A. Sarkar, L. Velasco, D. Wang, Q. Wang, G. Talasila, L. de Biasi, C. Kübel, T. Brezesinski, S. S. Bhattacharya, H. Hahn and B. Breitung, *Nature Communications*, 2018, **9**, 3400.

31. T. X. Nguyen, J. Patra, J.-K. Chang and J.-M. Ting, *Journal of Materials Chemistry A*, 2020, **8**, 18963-18973.

32. C. Zhao, F. Ding, Y. Lu, L. Chen and Y.-S. Hu, *Angewandte Chemie International Edition*, 2020, **59**, 264-269.

33. N. Qiu, H. Chen, Z. Yang, S. Sun, Y. Wang and Y. Cui, *Journal of Alloys and Compounds*, 2019, **777**, 767-774.

34. G. Ma, S. Li, W. Zhang, Z. Yang, S. Liu, X. Fan, F. Chen, Y. Tian, W. Zhang and S. Yang, *Angewandte Chemie International Edition*, 2016, **55**, 3667-3671.

35. M. Casas-Cabanas, M. Reynaud, J. Rikarte, P. Horbach and J. Rodriguez-Carvajal, *J Appl Crystallogr*, 2016, **49**, 2259-2269.

36. R. Shunmugasundaram, R. S. Arumugam and J. R. Dahn, *Journal of the Electrochemical Society*, 2016, **163**, A1394-A1400.

37. J. Rodriguez-Carvajal, T. Roisnel, A. Daoud-Aladine and A. Bouvet, *Acta Crystallogr A*, 1999, **55**, 262-263.

38. J. S. Serrano-Sevillano, M. Reynaud, A. Saracibar, T. Altantzis, S. Bals, G. van Tendeloo and M. C. Casas-Cabanas, *Phys Chem Chem Phys*, 2018, **20**, 23112-23122.

39. A. S. Menon, S. Khalil, D. O. Ojwang, K. Edstrom, C. P. Gomez and W. R. Brant, *Dalton T*, 2022, **51**, 4435-4446.

40. B. H. Toby and R. B. J. J. o. A. C. Von Dreele, 2013, **46**, 544-549.

41. M. Newville, *J. Synchrotron Radiat.*, 2001, **8**, 322-324.

42. B. Ravel and M. Newville, *J. Synchrotron Radiat.*, 2005, **12**, 537-541.

43. B. Ravel and M. J. J. o. s. r. Newville, 2005, **12**, 537-541.

44. J. J. Rehr, J. Mustre de Leon, S. I. Zabinsky and R. C. Albers, *J. Am. Chem. Soc.*, 1991, **113**, 5135.

45. B. Ravel and M. J. Newville, *J. Synchrotron Radiat.*, 2005, **12**, 537-541.

46. M. Reynaud, J. Serrano-Sevillano and M. Casas-Cabanas, *Chem Mater*, 2023, **35**, 3345-3363.

47. C. Delmas, M. Ménétrier, L. Croguennec, I. Saadoune, A. Rougier, C. Pouillerie, G. Prado, M. Grüne and L. Fournès, *Electrochim Acta*, 1999, **45**, 243-253.

48. Z. J. Cai, H. W. Ji, Y. Ha, J. Liu, D. H. Kwon, Y. Q. Zhang, A. Urban, E. E. Foley, R. Giovine, H. Kim, Z. Y. Lun, T. Y. Huang, G. B. Zeng, Y. Chen, J. Y. Wang, B. D. McCloskey, M. Balasubramanian, R. J. Clement, W. L. Yang and G. Ceder, *Matter-Us*, 2021, **4**, 3897-3916.

49. J. M. Tarascon, W. R. Mckinnon, F. Coowar, T. N. Bowmer, G. Amatucci and D. Guyomard, *Journal of the Electrochemical Society*, 1994, **141**, 1421-1431.

50. M. Vaarkamp, *Catalysis Today*, 1998, **39**, 271-279.

51. M. D. Radin, S. Hy, M. Sina, C. Fang, H. Liu, J. Vinckeviciute, M. Zhang, M. S. Whittingham, Y. S. Meng and A. Van Der Ven, *Advanced Energy Materials*, 2017, **7**, 1602888.

52. E.-S. Lee, A. Huq, H.-Y. Chang and A. Manthiram, *Chem Mater*, 2012, **24**, 600-612.

53. E.-S. Lee, K.-W. Nam, E. Hu and A. Manthiram, *Chem Mater*, 2012, **24**, 3610-3620.

54. K. A. Jarvis, C. C. Wang, A. Manthiram and P. J. Ferreira, *Journal of Materials Chemistry A*, 2014, **2**, 1353-1362.

55. A. R. Armstrong, M. Holzapfel, P. Novák, C. S. Johnson, S.-H. Kang, M. M. Thackeray and P. G. Bruce, *Journal of the American Chemical Society*, 2006, **128**, 8694-8698.

The data supporting this article have been included as part of the Supplementary Information.